GDCh Research Article Angewandte International Edition Chemie www.angewandte.org

How to cite: *Angew. Chem. Int. Ed.* **2024**, *63*, e202412188
doi.org/10.1002/anie.202412188

CO_2 Reduction

Supramolecular Anchoring of Fe(III) Molecular Redox Catalysts into Graphitic Surfaces Via CH-π and π–π Interactions for CO_2 Electroreduction

Zhi-Mei Luo, Jia-Wei Wang, Marco Nicaso, Marcos Gil-Sepulcre, Eduardo Solano, Vasilis Nikolaou, Jordi Benet, Mireia Segado-Centellas, Carles Bo, and Antoni Llobet**

Abstract: Photoelectrochemical devices require solid anodes and cathodes for the easy assembling of the whole cell and thus redox catalysts need to be deposited on the electrodes. Typical catalyst deposition involves drop casting, spin coating, doctor blading or related techniques to generate modified electrodes where the active catalyst in contact with the electrolyte is only a very small fraction of the deposited mass. We have developed a methodology where the redox catalyst is deposited at the electrode based on supramolecular interactions, namely CH-π and π–π between the catalyst and the surface. This generates a very well-defined catalysts-surface structure and electroactivity, together with a very large catalytic response. This approach represents a new anchoring strategy that can be applied to catalytic redox reactions in heterogeneous phase and compared to traditional methods involves about 4–5 orders of magnitude less mass deposition to achieve comparable activity and with very well-behaved electroactivity and stability.

Introduction

The catalytic transformation of CO_2 into reduced products such as CO, CH_2CH_2 or EtOH[1–3] is an important task nowadays given its implications in the mitigation of global warming[4] generating solar fuels[5] and/or the generation of valued added chemicals.[6] Thus, CO_2 reduction reaction (CO_2RR) is a key reaction since it can lead to C-neutral fuels as well as valuable C1 and C2 hydrocarbon building blocks useful as synthons for the chemical industry,[1,3, 7–10] using sunlight as the only external input.[11–14] In this context photoelectrochemical cells (PEC) are useful devices[15] that can achieve this, provided that the CO_2RR is coupled to an oxidation reaction such that of for instance lignin[16] or water[17]. For this purpose, efficient and selective catalysts are needed both for the oxidation and reduction reactions to generate useful devices. Further, from a technological perspective the use of solid state (photo)anodes and photo-(cathodes) greatly simplifies the construction of these devices and thus is highly desired.[2,18–21] The electrocatalytic CO_2RR can be achieved using molecular[22] or solid state[23] catalyst and in both cases a critical issue will be anchoring of the catalyst into the corresponding conductive or semi-conductive surface since it will determine the electronic communication between them as well as their long-term stability.

Robust, efficient and selective molecular CO_2RR have been described based on transition metal complexes containing macrocyclic ligands with π-extended systems such as phthalocyanines,[24–26] porphyrins[2,27] and other type of acyclic ligands.[28–29]

Anchoring strategies for molecular CO_2RR catalyst into surfaces involve the use of covalent[30] or π–π interactions[22] by functionalizing the surface and/or the catalyst or both. The strategy will be highly dependent on the nature of the surface where the catalyst will be deposited. An additional strategy consists on depositing a dispersion or solution of the catalyst on top of the surface and evaporate the solvent using the well know techniques of drop casting,[22] spin coating[3] or doctor blading[31] among others. Further the use of insoluble conductive polymers such as polypyrrole[32] or polythiophene[33] has also been proven to be effective.

We have recently developed a new strategy to anchor molecular catalyst into graphitic surfaces that involves supramolecular bonding including CH-π interactions[11,19, 34–35] that have proven to be extremely useful.

[*] Z.-M. Luo, Dr. J.-W. Wang, M. Nicaso, Dr. M. Gil-Sepulcre, Dr. V. Nikolaou, Dr. J. Benet, M. Segado-Centellas, Prof. Dr. C. Bo, Prof. Dr. A. Llobet
Institute of Chemical Research of Catalonia (ICIQ), Barcelona Institute of Science and Technology (BIST), Tarragona 43007, Spain
E-mail: cbo@iciq.cat
allobet@iciq.cat

Dr. E. Solano
NCD-SWEET beamline, ALBA synchrotron light source. Carrer de la Llum, 2, 26, 08290 Cerdanyola del Vallès, Barcelona

M. Segado-Centellas, Prof. Dr. C. Bo
Departament de Quíimica Física i Inorgànica, Universitat Rovira i Virgili, Marcel·lí Domingo s/n, 43007 Tarragona, Spain

Here on, we report the supramolecular anchoring into carbon fiber paper ($\mathbf{C_{FP}}$) graphitic electrodes of two Fe(III) complexes containing the deprotonated porphyrin ligands 5,10,15,20-tetraphenylporphyrin (**H_2TPP**) and 5,10,15,20-tetra([1,1′-biphenyl]-4-yl)porphyrin (**H_2TbPP**) named as **FeTPP** and **FeTbPP**, respectively (see drawn structures in Scheme 1). The new molecular hybrid materials generated are labelled as **FeTPP@C_{FP}** and **FeTbPP@C_{FP}** and their characterization and performance as CO_2RR catalysts reported by means of spectroscopic and electrochemical techniques and complemented with DFT calculations. We further describe the benefits of the supramolecular strategy versus simple drop casting techniques.

Results

Structure and Activity in Homogeneous Phase in NMP

FeTbPP was synthesized as a Fe(III) complex by complexation of the free base **H_2TbPP** with $FeBr_2$, and then characterized by single-crystal X-ray diffraction (Figure 1 and Table S1, CCDC number 2306490), UV/Vis absorption spectroscopy (Figure S1) and high-resolution mass spectroscopy (Figure S2a). The electrocatalytic properties of **FeTPP** and **FeTbPP** were studied by cyclic voltammetry in homogeneous phase in *N*-methyl-2-pyrrolidone (NMP) as solvent, given the good solubility of both complexes in NMP (solubility max.: 14.7 mM for **FeTPP**; 0.94 mM for **FeTbPP** at 25 °C). Figure 2a and Figure S3 show their cyclic voltammograms (CVs) in NMP using a glassy carbon disc as a working electrode and NBu_4PF_6 as a supporting electrolyte. The behavior of **FeTPP** is comparable to the one already described for this complex in DMF,[36] where three 1-electron redox processes are observed under Ar in the potential range of −0.5 to -2.5 V, associated with Fe(III)/Fe(II) (−0.72 V), Fe(II)/(I) (−1.55 V) and Fe(I)/Fe(0) (−2.19 V) couples. For the purpose of easy electron counting, we will use formal Fe oxidation states, although it is obvious that at low oxidation states electron reduction can also occur at the ligand.[37] All the redox potentials are referred to ferrocene in organic solvents and *vs.* NHE in aqueous solutions. For the case of **FeTbPP** the behavior is also similar indicating that the replacement of phenyls at the meso positions by biphenyls does not strongly influence the electron density at the metal center. However, the Fe(I)/Fe(0) redox couple for **FeTbPP** appears at −2.15 V, anodically shifted by 40 mV with regard to that of **FeTPP**, indicating a higher degree of aromatic delocalization or the former ligand system. As a consequence of this in the presence of CO_2 and 1 M PhOH the **FeTbPP** has a slightly larger activity at low overpotentials as can be observed in the Tafel plots of Figure 2b inset but the maximum turnover frequency (TOF_{max}) is lower (3.8×10^3 s^{-1} for **FeTPP** and 0.3×10^3 s^{-1} for **FeTbPP)**.

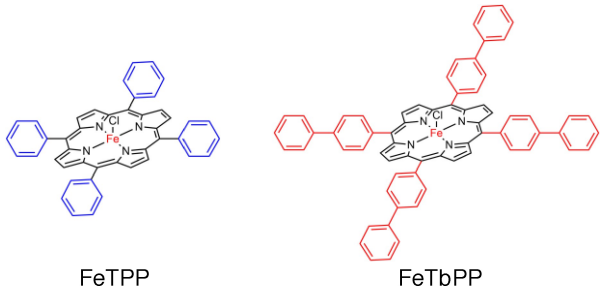

Scheme 1. Chemical structures of **FeTPP** and **FeTbPP**.

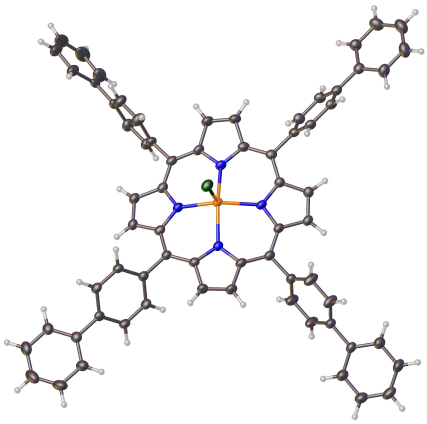

Figure 1. Ortep plot of the X-ray structure of **FeTbPP**, with ellipsoids drawn at 30% probability. Color: Fe, orange; C, black; N, blue; Cl, green; H, gray.

Supramolecular Anchoring on Graphitic Surfaces

Activated carbon fiber papers ($\mathbf{C_{FP}}$) were used as working electrodes (see Supporting Information for washing and activation protocols) to anchor the iron porphyrins, **FeTbPP** and **FeTPP** via supramolecular interactions. The $\mathbf{C_{FP}}$ electrodes were dipped into a 0.5 mM solution of the Fe porphyrin complexes for 7 days without stirring and then removed from the solution and thoroughly rinsed with MeOH and air dried. This generated new hybrid molecular materials were labelled as **FeTPP@C_{FP}** and **FeTbPP@C_{FP}**. The kinetics of mass deposition on the electrode over time were monitored by cyclic voltammetry with plotting the $j_{a,p}$ at −0.15 V *vs.* *t* and the capacitance measured −0.35 V as

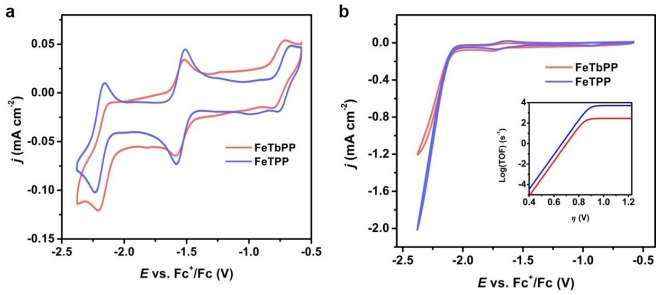

Figure 2. CVs of 0.5 mM **FeTPP** (blue trace) and **FeTbPP** (red trace) in 0.1 M $TBAPF_6$ dissolved in NMP (a) under Ar; (b) with 1.0 M phenol under CO_2. Inset in (b): Tafel plots. Same color code for all graphs.

shown in Figure 3. The mass deposition was quantitively analyzed via cyclic voltammetry in 0.5 M $KHCO_3$ aqueous solution by integrating the charge under the Fe(III)/Fe(II) redox wave (see Supporting Information for the quantitative analysis; Figure S4) which gives a value of 3.1 nmol/cm^2. The deposition of **FeTbPP** was also carried out on a glassy carbon plate (**GC_P**) using a saturated solution of the complex in NMP in order to maximize mass deposition. In this way we obtained a **FeTbPP@GC_P** electrode with a Γ= 16 pmol/cm^2 that implies a surface coverage of 65 % (see Figure S5 and Supporting Information for details). A similar process was used for the anchoring of **FeTPP** on **C_{FP}** electrodes (Figure S6) to generate **FeTPP@C_{FP}**, giving a mass deposition of 0.20 nmol/cm^2 (Figure S7) that is about 15 times (3.1/ 0.2 = 15.5) lower than for the case of the biphenyl substituted porphyrin, clearly manifesting the role of the biphenyl in the anchoring process. As determined by inductively coupled plasma mass spectrometry (ICP-MS), the bulk loadings of iron porphyrins are 2.6 and 0.6 nmol cm^{-2} at the **FeTbPP@C_{FP}** and **FeTPP@C_{FP}** samples, respectively, in relatively good agreement with the CV-determined loading values. The decrease on mass deposition at the electrode is a consequence of both the higher solubility of the **FeTPP** complex *vs.* that of **FeTbPP** in NMP and the capacity of the latter to achieve supramolecular interactions that give a larger binding strength with the graphitic surface, as will be discussed in the next section. Notably, this strategy is applicable to other metal analogs, as exemplified by the Co-based one (**CoTbPP**, see synthesis and characterization Figure S2b in SI). By applying the same protocol used for **FeTbPP@C_{FP}**, we could obtain supramolecularly anchored **CoTbPP** on **C_{FP}** (Figure S8).

Electrochemical Performances of the Hybrid Materials

The electrochemical performance of the hybrid material using the supramolecular and the drop casting anchoring strategies were evaluated based on electrical impedance spectroscopy (EIS), CV and Coulombimetric techniques.

Figure 4a shows the EIS spectra obtained for **FeTbPP@C_{FP}** (Γ=1.5 nmol/cm^2) and **FeTbPP/C_{FP}** (Γ=400 nmol/cm^2) under CO_2 in 0.5 M $KHCO_3$ in aqueous solution at −1.10 V *vs.* NHE. The results shown were simulated with a solution resistance (R_s, ohmic resistance) in the high-frequency region and the charge-transfer resistances (R_{ct}) controlling the kinetics at the electrode interface using the circuit displayed in Figure 4a and by extracting the semi-circle diameter.[38] The R_s values of both samples are similar (ca. 10 Ω), while the R_{ct} for **FeTbPP@C_{FP}** is 20 Ω and for **FeTbPP/C_{FP}** is 680 Ω, revealing a much faster charge transport for the supramolecular methodology over drop casting at the electrocatalytic event. This agrees with the monolayer nature of supramolecularly deposited catalyst as opposed to the drop casted one that will have additional resistances due to the multilayer nature of the material obtained in this manner.

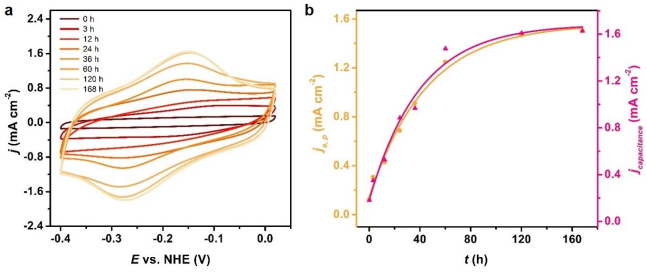

Figure 3. Mass deposition over time monitored by electrochemical techniques of a 0.5 mM solution of **FeTbPP** in NMP in the presence of 1.0×1.0 cm^2 **C_{FP}** electrode. Left, CVs of the rinsed electrode in a fresh electrolyte 0.5 M $KHCO_3$ solution. Right, plots of $j_{a,p}$ at −0.15 V for the Fe(III)/Fe(II) couple (yellow trace) and the capacitive current (pink trace) measured at −0.35 V.

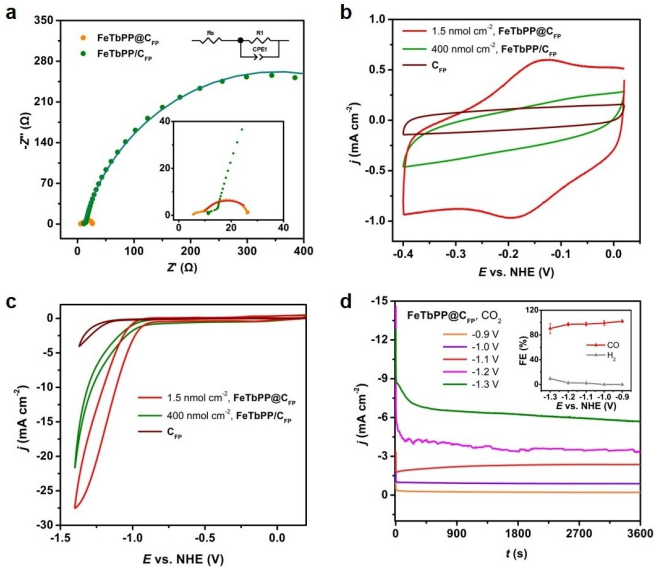

Figure 4. Electrochemical performance of the **FeTbPP** complex anchored on **C_{FP}** via supramolecular interactions, **FeTbPP@C_{FP}** (1.5 nmol/cm^2; red traces) and by drop casting, **FeTbPP/C_{FP}** (400 nmol/cm^2; green traces). (a) EIS measurements were conducted over a frequency range of 0.005 Hz to 100 kHz at −1.10 V *vs.* NHE under CO_2 in 0.5 M $KHCO_3$ solution. (b) CVs in the range of 0 to −0.40 V, (c) CV in the range of 0 to −1.40 V under CO_2 0.5 M $KHCO_3$ solutions and (d) j vs. t traces of the bulk electrolysis performed for **FeTbPP@C_{FP}** at an E_{app} = −0.90 (orange), −1.00 (purple), −1.10 (red), −1.20 (pink) and −1.30 V (green). Inset in (d) shows the product distribution and Faradaic Efficiencies for the CO and H_2 generated.

Further the supramolecular and drop casted electrodes were analyzed by CV in the 0.0 to −0.4 V range in a 0.5 M $KHCO_3$ aqueous solution under Ar and the CVs are exhibited in Figure 4b. For the **FeTbPP@C_{FP}** electrode the Fe(III)/Fe(II) couple is perfectly observed at the same potential as it appears in homogeneous phase, indicating the nature of the catalyst remains intact after anchoring. In sharp contrast, in the CV of the drop casted catalyst material, **FeTbPP@C_{FP}**, the Fe(III)/Fe(II) redox wave is not observed even if the mass deposited is 266 times (400/1.5) that of the supramolecular material. Once again this highlights the benefit of a precise deposition control of the

catalyst species on the surface of the electrode with a well-defined and homogeneous manner.

Figure 4c presents the performance of these hybrid materials for the electrocatalytic CO_2RR in 0.5 M $KHCO_3$ solutions. Again, the supramolecularly modified electrode **FeTbPP@C$_{FP}$** is better defined and outperforms the drop casted one, **FeTbPP/C$_{FP}$**, even containing 266 times less mass of catalyst. For instance, at −1.25 V the current density obtained for the supramolecular anchoring is 22 mA/cm^2 whereas for the drop casted is 8 mA/cm^2. Thus, at an E_{app} = −1.25 V the electrocatalytic current density is 2.75 (22/8) times larger for the supramolecular case than for the drop casted. Since in drop casted case, the amount of mass deposited is 366 (400/1.5) times larger; it follows that the number of active sites in the drop casted case responsible for catalysis at this potential is of approximately 1 out 1000 (2.75×366).

Finally, bulk electrolysis experiments were carried out with **FeTbPP@C$_{FP}$** at an E_{app} = −0.9, −1.0, −1.1, −1.2 and −1.3 V and the *"j vs. t"* plots are shown in Figures 4d, displaying very stable currents and with TOF at 1 h of 1.2, 4.6, 7.6, 12.6 and 20 s^{-1}, respectively (Figure 4d and Table S2). The product distribution analysis is presented in Figure 4d inset, showing very high selectivity towards CO formation over H_2, and with FE reaching close to 100 % at E_{app} = −0.9 ~ −1.2 V. The durability was further confirmed by an extended electrolysis for 2 h at −1.1 V with **FeTbPP@C$_{FP}$**, where the CO Faradaic efficiency of the system decreased a bit till 95 % (Figure S9). The slight decrease in performance can be partially attributed to the consumption of CO_2 decreasing its concentration. The hybrid materials were also characterized by resonance Raman spectroscopies (Figure S10), scanning electron microscopy (SEM; Figure S11) and X-ray photoelectron spectroscopy (XPS; Figure S12) and the results are reported in the SI. We can see that after electrolysis, no additional iron species like FeO_x could be detected by XPS (Figure S12b).

Table 1 reports the electrocatalytic CO_2RR performance of several Fe and Co porphyrin complexes that have been anchored into graphitic supports for comparative purposes. Entry 2 and 3[39] contain two complexes with identical active site as **FeTbPP** and give lower values of TOF than the latter, and thus can be associated with the availability of active sites within the anchoring methodology. Entry 4[40] contains an Fe porphyrin with quaternary ammonium substituents that provokes a positive shift of 200 mV compared to **FeTPP**[41] regarding their Tafel plots. Even under these conditions the **FeTbPP@C$_{FP}$** material outperforms the ammonium substituted Fe complex in term of TOF even considering the same applied potential. Finally, entries 5–7[42–44] contain 3 Co porphyrin complexes whose performances are clearly inferior to that of **FeTbPP@C$_{FP}$**.

For the case of the **FeTPP@C$_{FP}$** electrode, the supramolecular strategy leads to a mass deposition of 0.2 nmol/cm^2. Due to this low coverage, the **FeTPP@C$_{FP}$** hybrid material displays a much lower catalytic currents than the **FeTbPP@C$_{FP}$**, and thus the bare electrode significantly competes with the molecular catalyst for the proton reduction reaction giving much lower selectivity (See Table S3 for additional details).

Structures of the Hybrid Materials

Synchrotron-based two-dimensional grazing incident wide angle X-ray scattering (2D GIWAXS) was used to characterize the structure and orientation of Fe porphyrin complex **FeTbPP** with the graphitic surfaces when deposited either via supramolecular interactions or by drop casting. For these experiments, we used a commercially available Si wafer coated with a single layer of graphene (denoted as **G$_r$**) labelled as **G$_r$-Si**. The **FeTbPP@G$_r$-Si** was prepared in the same manner as described previously for the **GC$_P$** whereas a diluted solution of **FeTbPP** in DCM was used for the drop casting obtaining the **FeTbPP/G$_r$-Si** electrode (see Supporting Information for protocols). Figure 5 displays the calibrated 2D GIWAXS patterns recorded for these hybrid materials. As can be observed, both, the **G$_r$-Si** and

Table 1: CO_2RR performances of selected Fe/Co porphyrins anchored on graphitic supports.[a]

Entry	Porphyrin structure	Substrate	Preparation	Loading (mol/cm^2)	Electrolyte	Main Product	TOF (s^{-1}) at E_{app} (V vs. RHE)	Ref.
1	**FeTbPP**	**C$_{FP}$**	Supra-molecular	1.5×10^{-9}	0.5 M $KHCO_3$	CO	20 at −0.87 7.6 at −0.67 1.2 at −0.47	This work
2	**FeCATPyr**	MWCNT	Drop cast	2.4×10^{-8}	0.5 M $NaHCO_3$	CO	0.04 at −0.6	[39]
3	**FeTAPP**	**C$_{FP}$**	Drop cast	5.4×10^{-7}	0.5 M $KHCO_3$	CO	9.75 at −0.9	[45]
4	**FeTMAP**	Graphene oxide	Electrostatic	4.2×10^{-9}	0.1 M $KHCO_3$	CO	0.8 at −0.39	[40]
5	**CoTPP**	MWCNT	Drop cast	3.4×10^{-9}	0.5 M $NaHCO_3$	CO	0.08 at −0.68	[43]
6	**CoTPP**	Modified graphene	Drop cast	1.0×10^{-8}	0.1 M $KHCO_3$	CO	2.75 at −0.87	[44]
7	**CoCh**	MWCNT	Drop cast	1.4×10^{-6}	5.0 mM, Na_2SO_4	CO	0.03 at −0.83	[42]

[a] Abbreviations: **FeCATPyr** = iron(III) chloride 5,10,15-tris(2,6-hydroxyphenyl)-20-(3-(pyren-1yl)propyl)porphyrin; **FeTAPP** = iron(III) chloride 5,10,15,20-tetrakis(4′-(1,3-diesteryl, 6-amino)azulenylphenyl)porphyrin; **FeTMAP** = 5,10,15,20-Tetrakis(4-trimethylammoniumphenyl)porphyrinato iron(III) pentachloride; **CoTPP** = cobalt(II) *meso*-tetraphenylporphyrin; **CoCh** = cobalt(II) chlorin; MWCNT = multiwalled carbon nanotubes.

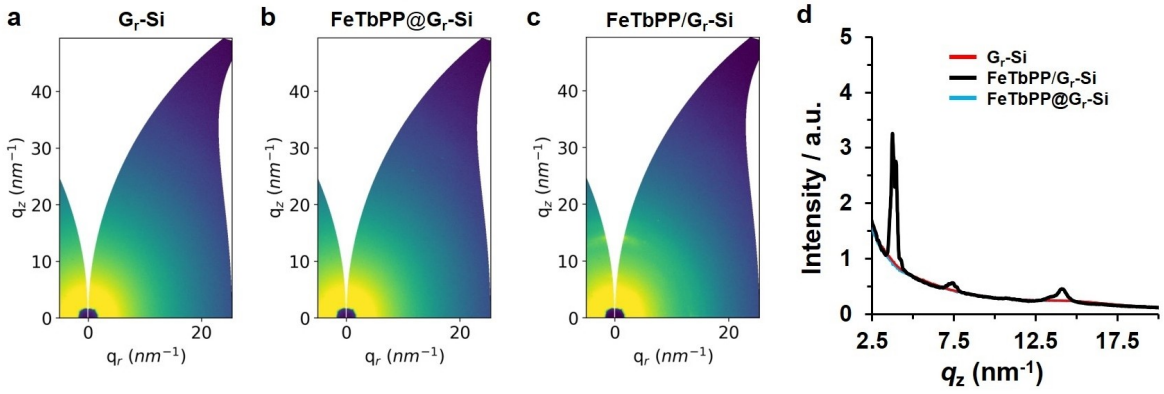

Figure 5. Recorded 2D GIWAXS patterns of (a) **G_r-Si**, (b) **FeTbPP@G_r-Si**, (c) **FeTbPP/G_r-Si** and (d) q_z profiles near the specular direction for the three electrodes.

FeTbPP@G_r-Si did not exhibit any characteristic signals beyond the background scattering. However, the Fe complex prepared via drop casting, i.e. **FeTbPP/G_r-Si**, presented scattering peaks from the multilayer parallel arrangement of **FeTbPP** units on top of the graphene surface.[46] The absence of characteristic signals from the **G_r-Si** and **FeTbPP@G_r-Si** indicates the absence of a multilayered system that can produce a Bragg peak, which corroborates the hypothesis of having a submonolayer of **FeTbPP** complex at the surface of the **G_r-Si** electrode. Complementarily, Figure 5d shows the plot of the azimuthal integrated intensity *vs.* $|q|$ of the calibrated 2D scattering patterns, where only the peaks from **FeTbPP/G_r-Si** located at 14.2, 7.5, 4.0 and 3.7 nm^{-1} were observed. By applying the reciprocal to real space transformation ($D \approx 2\pi/q$) we obtained real distances of 4.4, 8.4, 15.6 and 16.8 Å. The preferential orientation of these scattering peaks is depicted as arc-shaped lines centered along the q_z direction, indicating a preference for a face-on orientation relative to the electrode surface.

DFT models including non-covalent interactions were built in order to further characterize these molecular hybrid materials using the BP86-D3[47] functional and the solvent model from consortium for small-scale modeling (COSMO; See SI, Figure S13 and S14 for details). The carbon-based electrode surface was reproduced using a sheet of graphene **G_r** containing 206 atoms (170 C and 36 H), whereas the Fe complexes were considered in their ground spin state $S = 5/2$. The calculated structure for **FeTPP** shows metric parameters very close to those observed by X-ray diffraction and thus validates the DFT model used here. The Fe porphyrin complexes **FeTPP** and **FeTbPP** were placed at the proximity of the **G_r** sheet and were allowed to adjust up to their maximum stabilization. Figures 6a-6b show the obtained structures for **FeTPP@G_r** and **FeTbPP@G_r** showing three types of interactions that include: a) CH-π (blue label) and b) π–π interactions (green label) between the *meso*-substituents and the graphene, as well as c) the π–π stacking between the Fe-porphyrin core and graphene (red label). Table 2 shows the anchoring energy obtained in each case. It is worth mentioning that the CH-π interactions described here by DFT have very similar distances as those observed experimentally in the packing X-ray structure of the **FeTbPP** complex (Figure 6c) that gives an interaction energy between the two molecules in the unit cell of −51.7 kcal/mol (Table 2).

Table 2: Calculated optimization energies of the Fe-porphyrin molecular hybrids anchored on graphene.

System	$E_{anchoring}$ (kcal mol^{-1})	$E_{rearrangement}$ (kcal mol^{-1})[c]
FeTPP@G_r	−146.8[a]	22.6
FeTbPP@G_r	−225.1[a]	28.0
$(FeTbPP)_2$@G_r, second layer	−99.1[b]	6.4
$(FeTbPP)_2$, crystal structure	−51.7[b]	N.A.

[a] $E_{anchoring} = E_{porphyrin\ on\ graphene} - (E_{porphyrin} + E_{graphene})$. [b] $E_{interaction} = E_{porphyrin\ assembling} - (E_{top\ porphyrin} + E_{bottom\ porphyrin})$. [c] $E_{rearrangement} = E_{anchored\ porphyrin} - E_{porphyrin}$, $E_{porphyrin}$ is the energy of the porphyrin free in solution and $E_{anchored\ porphyrin}$ is the energy of the porphyrin in its anchored geometry but without graphene.

Further, the presence of the additional phenyl rings in **FeTbPP@G_r** compared to **FeTPP@G_r** clearly increases the supramolecular affinity for the graphene surface resulting in an anchoring energy enhancement of −78.3 kcal/mol (Table 2). The spin density associated with the supramolecular anchoring is depicted in Figure 6d for **FeTbPP@G_r**. An interesting aspect of this bonding between the graphene surface and the **FeTbTPP** complex is that involves a distortion mainly on the biphenyl moiety of 28 kcal/mol with regard to its ideal structure dielectrically corrected for MeOH (Table 2). This distortion allows to maximizes the π–π interaction with the graphitic surface while maintaining the CH-π interaction.

Figure 6e shows the packing of a second layer of the Fe porphyrin complex labeled as **$(FeTbPP)_2$@G_r**, mainly via Van de Waals interactions with a bonding energy of −99.1 kcal/mol (Table 2). Assuming that the **FeTPP** barely anchors at the surface of the graphite electrode and its anchoring energy is −146.8 kcal/mol, it suggests that the second layer doesn't anchor in the supramolecular strategy

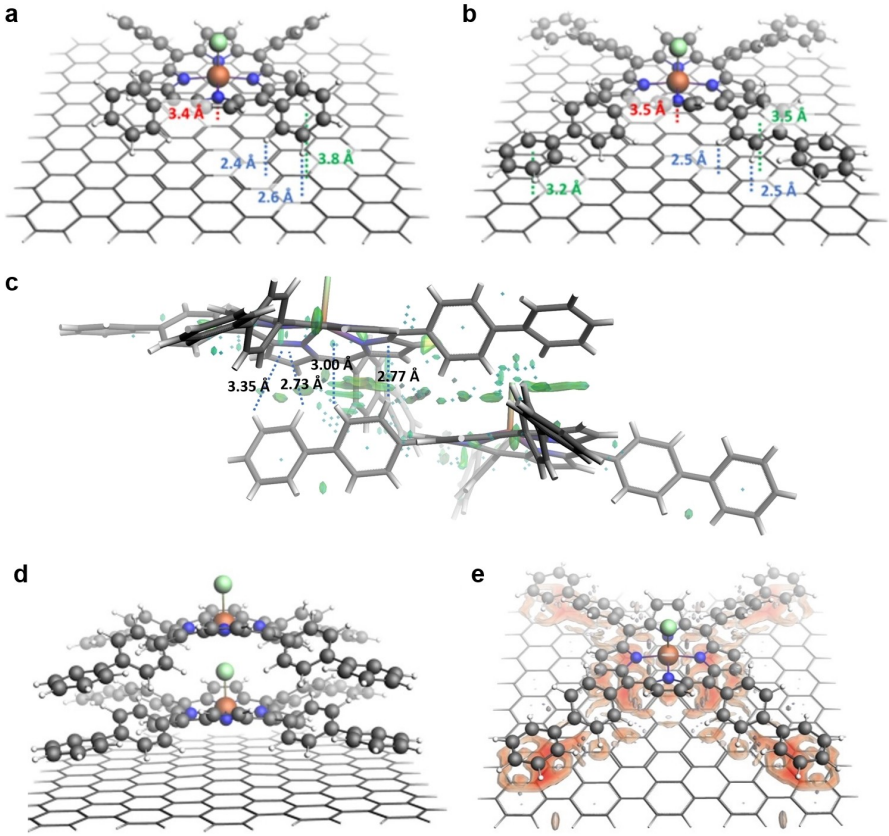

Figure 6. DFT calculate structures for (a) **FeTPP@G$_r$** and (b) **FeTbPP@G$_r$**. (c) Details of the CH-π interactions in the packed structure of **FeTbPP** calculated by using the crystallographic xyz coordinates, including the electron density map. (d) DFT calculate structure of **(FeTbPP)$_2$@G$_r$**. (e) Spin density mapping showing the interactions of the graphitic surface with the Fe porphyrin in **FeTbPP@G$_r$**. Metric parameters for the supramolecular interactions are shown in red, green for π–π interactions and blue for CH-π interactions (c-d).

and only can occur when using the drop casting methodology.

It is interesting to realize here that the main distances between the central points of the best planes described by the tetrapyrrole cores of the porphyrin and the graphene sheet are 3.6 and 8.4 Å that agree relatively well with the values obtained by GIWAXS that are 4.4 and 8.4 Å, respectively. The first computed layer appears 0.4 Å shorter than obtained experimentally, that might indicate a slight overestimation of bond strength obtained by DFT. On the other hand, the second layer distances match very well with the experimental value.

Discussion and Conclusions

We report the electrocatalytic properties of **FeTPP** and **FeTbPP** in NMP solution and anchored on graphitic electrodes as well as a detailed analysis of their relative affinity for these graphitic substrates. The biphenyl groups in **FeTbPP** do not modify the intrinsic electron density of the Fe center neither of the 2nd coordination sphere with regard to **FeTPP**, and thus the redox properties of two catalysts are very similar in terms of the potentials of their couples in absence of catalysis neither in their electrocatalytic properties towards CO_2RR in the presence of a proton source (TOF_{max} for **FeTPP** and **FeTbPP** is 3.8×10^3 and 0.3×10^3 s^{-1}, respectively). While the biphenyl substitution at the meso position of the porphyrin ligand does not modify the properties of metal center it changes significantly the solubility in organic solvents such as NMP. As a result of this **FeTbPP** decreases its solubility with regard to **FeTPP** by a factor of 15 approximately. This in turn is beneficial for the supramolecular anchoring since the supramolecular mass deposition depends on both the affinity to generate bonds with the graphitic surface but also the catalyst solubility in the solvent used.

Given the nature of the supramolecular interaction between the **FeTbPP** catalyst and the surface only a monolayer of the catalyst is attached to the surface. This is supported by the 65 % surface coverage on 2D glassy carbon plates, **GC$_p$**, and corroborated by the absence of response in GIWAXS and by DFT analysis where the energy of depositing a second layer dramatically decreases with regard to the first one, and is significantly lower than that of **FeTPP**. Further the high selectivity of the hybrid material **FeTbPP@C$_{FP}$**, to CO indicates that the coverage of the electrode is high otherwise as reflected in the **FeTPP@C$_{FP}$** case the activity of the electrode generates an important amount of H_2 together with CO (Tables S2 and S3). In

addition, compared to related examples in the literature with different anchoring strategies shown in Table 1, **FeTbPP@C$_{FP}$** displays larger TOF indicating that all Fe deposited at the surface are active as expected for a monolayer.

It is interesting to see that in order to maximize the supramolecular π–π and CH-π interaction, the C–C angle bonding the two meso-substituted phenyl groups in **FeTbPP**, are significantly distorted with regard to the calculated model using the solvation dipole for MeOH. Even though this distortion which involves 28 kcal/mol is highly compensated by the bonding energy with graphene that is 225 kcal/mol.

The supramolecular anchoring protocol used here involves the use of NMP where the two catalysts **FeTbPP** and **FeTPP** are soluble, and is governed by a slow equilibrium (168 h to completion) that involves the catalyst attachment at the surface in with the one that remains in solution.

$$\textbf{FeTbPP}_{(l)} + \text{Surface}_{(s)} = \textbf{FeTbPP}\text{-Surface}_{(s)} \quad (1)$$

Thus, once the hybrid material **FeTbPP@C$_{FP}$** is introduced in a fresh solution of NMP, the equilibrium will be slowly re-established and part of the Fe catalyst will be solubilized. However, if the hybrid material is introduced in a solvent where the catalyst is insoluble, such as water, then the hybrid material remains extraordinarily stable.

The benefits of the present supramolecular strategy versus other methodologies and specially *vs.* drop casting, is the well-defined and homogeneous nature of the catalyst over the whole surface. For the drop casted case different Fe sites due to aggregation will be generated that will imply a different electrochemical response. Further, a large amount of the Fe deposited by drop casting (1 out of 1000) are electrochemically silent as discussed earlier. In addition, the lower resistance observed by EIS for the supramolecular interaction also reflects a single type of a unique Fe center as a monolayer and with fast interfacial electron transfer kinetics.

An additional outcome of the benefit of our anchoring strategy is manifested in the clearly observed redox wave at −0.5 V that is not seen in the drop casted case, even if in the latter there are 335 times more Fe deposited at the electrode. Finally, it is interesting to realize that the **FeTbPP@C$_{FP}$** hybrid material presents the largest TOF reported in the literature under similar conditions (pH, applied potential, solvent, proton source, supporting electrolyte, etc.) compared to other anchoring strategies with the same or similar active sites as indicate in Table 1. Since with the supramolecular anchoring technique all deposited Fe complexes are active, then it could be taken as a reference measurement of the ratio of active sites *vs.* catalyst deposited, in the ones using other anchoring strategies.

Overall, we have presented a very convenient model for supramolecular anchoring including CH-π and π–π interactions, between iron porphyrin catalysts and graphitic surfaces, enabling a high-performance molecular electrode for aqueous CO_2 electroreduction.

Supporting Information

The authors have cited additional references within the Supporting Information.[22,47–62]

Acknowledgements

Z.-M.L. and M.N. acknowledge the award of a PhD grant from ICIQ (PID2019-111617RB–I00) and MICINN Severo Ochoa (PES2020-093521), respectively. A.L. acknowledges MICINN through project PID2022-140143OB–I00 and Generalitat the Catalunya for the project 2017 SGR 1631. C.B. acknowledges MICINN through project PID2020-112806RB–I00 (MCIN/AEI/10.13039/501100011033) and Generalitat the Catalunya for the project SGR 01583. A.L. and C.B. are grateful to the Severo Ochoa Excellence Accreditation 2020 – 2023 (CEX2019-000925-S, MCI/AEI) the ICIQ Foundation, and the CERCA Program of the Generalitat de Catalunya. GIWAXS data was recorded at NCD-SWEET beamline at ALBA synchrotron with the collaboration of ALBA staff

Conflict of Interest

The authors declare no conflict of interest.

Data Availability Statement

The data that support the findings of this study are available in the supplementary material of this article.

Keywords: supramolecular interaction · CO_2 reduction · iron porphyrin · molecular hybrid materials · CH-π interaction

[1] Y. Cheng, P. Hou, X. Wang, P. Kang, *Acc. Chem. Res.* **2022**, *55*, 231–240.
[2] M. Wang, V. Nikolaou, A. Loiudice, I. D. Sharp, A. Llobet, R. Buonsanti, *Chem. Sci.* **2022**, *13*, 12673–12680.
[3] C. Chen, S. Yu, Y. Yang, S. Louisia, I. Roh, J. Jin, S. Chen, P.-C. Chen, Y. Shan, P. Yang, *Nat. Catal.* **2022**, *5*, 878–887.
[4] Z. Liu, D. Guan, W. Wei, S. J. Davis, P. Ciais, J. Bai, S. Peng, Q. Zhang, K. Hubacek, G. Marland, R. J. Andres, D. Crawford-Brown, J. Lin, H. Zhao, C. Hong, T. A. Boden, K. Feng, G. P. Peters, F. Xi, J. Liu, Y. Li, Y. Zhao, N. Zeng, K. He, *Nature* **2015**, *524*, 335–338.
[5] E. A. Reyes Cruz, D. Nishiori, B. L. Wadsworth, N. P. Nguyen, L. K. Hensleigh, D. Khusnutdinova, A. M. Beiler, G. F. Moore, *Chem. Rev.* **2022**, *122*, 16051–16109.
[6] M. Aresta, A. Dibenedetto, A. Angelini, *Chem. Rev.* **2014**, *114*, 1709–1742.
[7] R. I. Masel, Z. Liu, H. Yang, J. J. Kaczur, D. Carrillo, S. Ren, D. Salvatore, C. P. Berlinguette, *Nat. Nanotechnol.* **2021**, *16*, 118–128.
[8] S.-F. Tang, X.-L. Lu, C. Zhang, Z.-W. Wei, R. Si, T.-B. Lu, *Sci. Bull.* **2021**, *66*, 1533–1541.

[9] J. W. Wang, Z. M. Luo, G. Yang, M. Gil-Sepulcre, S. Kupfer, O. Rudiger, G. Ouyang, *Proc. Natl. Acad. Sci. USA* **2024**, *121*, e2319288121.
[10] W. L. Zhang, H. H. Huang, Z. M. Luo, F. Ma, S. Gonell, Z. F. Ke, L. Tan, J. W. Wang, *ChemSusChem* **2024**, *17*, e202301113.
[11] J.-W. Wang, M. Gil-Sepulcre, H.-H. Huang, E. Solano, Y.-F. Mu, A. Llobet, G. Ouyang, *Cell Rep. Phys. Sci.* **2021**, *2*, 100681.
[12] J. W. Wang, F. Ma, T. Jin, P. He, Z. M. Luo, S. Kupfer, M. Karnahl, F. Zhao, Z. Xu, T. Jin, T. Lian, Y. L. Huang, L. Jiang, L. Z. Fu, G. Ouyang, X. Y. Yi, *J. Am. Chem. Soc.* **2023**, *145*, 676–688.
[13] F. Ma, Z.-M. Luo, J.-W. Wang, B. M. Aramburu-Trošelj, G. Ouyang, *Coord. Chem. Rev.* **2024**, *500*, 215529.
[14] F. Ma, Z. M. Luo, J. W. Wang, G. F. Ouyang, *J. Am. Chem. Soc.* **2024**, *146*, 17773–17783.
[15] A. Nakada, H. Kumagai, M. Robert, O. Ishitani, K. Maeda, *Acc. Mater. Res.* **2021**, *2*, 458–470.
[16] J. Bi, Q. Zhu, W. Guo, P. Li, S. Jia, J. Liu, J. Ma, J. Zhang, Z. Liu, B. Han, *ACS Sustainable Chem. Eng.* **2022**, *10*, 8043–8050.
[17] V. Andrei, G. M. Ucoski, C. Pornrungroj, C. Uswachoke, Q. Wang, D. S. Achilleos, H. Kasap, K. P. Sokol, R. A. Jagt, H. Lu, T. Lawson, A. Wagner, S. D. Pike, D. S. Wright, R. L. Z. Hoye, J. L. MacManus-Driscoll, H. J. Joyce, R. H. Friend, E. Reisner, *Nature* **2022**, *608*, 518–522.
[18] R. Matheu, I. A. Moreno-Hernandez, X. Sala, H. B. Gray, B. S. Brunschwig, A. Llobet, N. S. Lewis, *J. Am. Chem. Soc.* **2017**, *139*, 11345–11348.
[19] M. A. Hoque, M. Gil-Sepulcre, A. de Aguirre, J. Elemans, D. Moonshiram, R. Matheu, Y. Shi, J. Benet-Buchholz, X. Sala, M. Malfois, E. Solano, J. Lim, A. Garzon-Manjon, C. Scheu, M. Lanza, F. Maseras, C. Gimbert-Surinach, A. Llobet, *Nat. Chem.* **2020**, *12*, 1060–1066.
[20] Y. Huang, H. Dai, D. Moonshiram, Z. Li, Z.-M. Luo, J.-H. Zhang, W. Yang, Y. Shen, J.-W. Wang, G. Ouyang, *J. Mater. Chem. A* **2023**, *11*, 2969–2978.
[21] J. S. Zhao, Y. F. Mu, L. Y. Wu, Z. M. Luo, L. Velasco, M. Sauvan, D. Moonshiram, J. W. Wang, M. Zhang, T. B. Lu, *Angew. Chem. Int. Ed.* **2024**, *63*, e202401344.
[22] X. Zhang, Y. Wang, M. Gu, M. Wang, Z. Zhang, W. Pan, Z. Jiang, H. Zheng, M. Lucero, H. Wang, G. E. Sterbinsky, Q. Ma, Y.-G. Wang, Z. Feng, J. Li, H. Dai, Y. Liang, *Nat. Energy* **2020**, *5*, 684–692.
[23] Z. Zhang, D. Wang, *J. Mater. Chem. A* **2022**, *10*, 5863–5877.
[24] J.-W. Wang, X. Zhang, L. Velasco, M. Karnahl, Z. Li, Z.-M. Luo, Y. Huang, J. Yu, W. Hu, X. Zhang, K. Yamauchi, K. Sakai, D. Moonshiram, G. Ouyang, *JACS Au* **2023**, *3*, 1984–1997.
[25] J. W. Wang, L. Jiang, H. H. Huang, Z. Han, G. Ouyang, *Nat. Commun.* **2021**, *12*, 4276.
[26] J. H. Wu, J. W. Wang, B. M. Aramburu-Troselj, F. J. Niu, L. J. Guo, G. F. Ouyang, *Nanoscale* **2024**, *16*, 11496–11512.
[27] M. Fang, L. Xu, H. Zhang, Y. Zhu, W. Y. Wong, *J. Am. Chem. Soc.* **2022**, *144*, 15143–15154.
[28] M. Wang, L. Chen, T. C. Lau, M. Robert, *Angew. Chem. Int. Ed.* **2018**, *57*, 7769–7773.
[29] J.-W. Wang, L.-Z. Qiao, H.-D. Nie, H.-H. Huang, Y. Li, S. Yao, M. Liu, Z.-M. Zhang, Z.-H. Kang, T.-B. Lu, *Nat. Commun.* **2021**, *12*, 813.
[30] J. Su, J.-J. Zhang, J. Chen, Y. Song, L. Huang, M. Zhu, B. I. Yakobson, B. Z. Tang, R. Ye, *Energy Environ. Sci.* **2021**, *14*, 483–492.
[31] D. Wang, J. Hu, B. D. Sherman, M. V. Sheridan, L. Yan, C. J. Dares, Y. Zhu, F. Li, Q. Huang, W. You, T. J. Meyer, *Proc. Natl. Acad. Sci. USA* **2020**, *117*, 13256–13260.
[32] J. M. Chen, W. J. Xie, Z. W. Yang, L. N. He, *ChemSusChem* **2022**, *15*, e202201455.
[33] M. Ventosa, M. Gil-Sepulcre, J. Benet-Buchholz, C. Gimbert-Suriñach, A. Llobet, *ACS Appl. Energ. Mater.* **2021**, *4*, 9775–9782.
[34] A. M. Beiler, A. Denisiuk, J. Holub, F. J. Sanchez-Baygual, M. Gil-Sepulcre, M. Z. Ertem, D. Moonshiram, A. Piccioni, A. Llobet, *ACS Energy Lett.* **2023**, *8*, 172–178.
[35] M. Gil-Sepulcre, J. O. Lindner, D. Schindler, L. Velasco, D. Moonshiram, O. Rudiger, S. DeBeer, V. Stepanenko, E. Solano, F. Wurthner, A. Llobet, *J. Am. Chem. Soc.* **2021**, *143*, 11651–11661.
[36] M. Hammouche, D. Lexa, M. Momenteau, J. M. Saveant, *J. Am. Chem. Soc.* **1991**, *113*, 8455–8466.
[37] C. Romelt, J. Song, M. Tarrago, J. A. Rees, M. van Gastel, T. Weyhermuller, S. DeBeer, E. Bill, F. Neese, S. Ye, *Inorg. Chem.* **2017**, *56*, 4746–4751.
[38] Z.-M. Luo, J.-W. Wang, J.-B. Tan, Z.-M. Zhang, T.-B. Lu, *ACS Appl. Mater. Interfaces* **2018**, *10*, 8231–8237.
[39] A. Maurin, M. Robert, *J. Am. Chem. Soc.* **2016**, *138*, 2492–2495.
[40] J. Choi, J. Kim, P. Wagner, S. Gambhir, R. Jalili, S. Byun, S. Sayyar, Y. M. Lee, D. R. MacFarlane, G. G. Wallace, D. L. Officer, *Energy Environ. Sci.* **2019**, *12*, 747–755.
[41] C. Costentin, M. Robert, J. M. Saveant, A. Tatin, *Proc. Natl. Acad. Sci. USA* **2015**, *112*, 6882–6886.
[42] S. Aoi, K. Mase, K. Ohkubo, S. Fukuzumi, *Chem. Commun.* **2015**, *51*, 10226–10228.
[43] X. M. Hu, M. H. Ronne, S. U. Pedersen, T. Skrydstrup, K. Daasbjerg, *Angew. Chem. Int. Ed.* **2017**, *56*, 6468–6472.
[44] J. Wang, X. Huang, S. Xi, H. Xu, X. Wang, *Angew. Chem. Int. Ed.* **2020**, *59*, 19162–19167.
[45] Y. Yuan, Y. Zhao, S. Yang, S. Han, C. Lu, H. Ji, T. Wang, C. Ke, Q. Xu, J. Zhu, X. Zhuang, *Chem. Commun.* **2022**, *58*, 1966–1969.
[46] Y. Xiao, X. Lu, *Materials Today Nano* **2019**, *5*, 100030.
[47] O. Salomon, M. Reiher, B. A. Hess, *J. Chem. Phys.* **2002**, *117*, 4729–4737.
[48] https://doi.org/10.19061/iochem-bd-1-296.
[49] M. Bursch, H. Neugebauer, S. Grimme, *Angew. Chem. Int. Ed.* **2019**, *58*, 11078–11087.
[50] P. Chakraborty, S. Purkait, S. Mondal, A. Bauzá, A. Frontera, C. Massera, D. Das, *CrystEngComm* **2015**, *17*, 4680–4690.
[51] M. Alvarez-Moreno, C. de Graaf, N. Lopez, F. Maseras, J. M. Poblet, C. Bo, *J. Chem. Inf. Model.* **2015**, *55*, 95–103.
[52] E. Caldeweyher, S. Ehlert, A. Hansen, H. Neugebauer, S. Spicher, C. Bannwarth, S. Grimme, *J. Chem. Phys.* **2019**, *150*, 154122.
[53] C. Bannwarth, S. Ehlert, S. Grimme, *J. Chem. Theory Comput.* **2019**, *15*, 1652–1671.
[54] Y. Okabe, S. K. Lee, M. Kondo, S. Masaoka, *J. Biol. Inorg. Chem.* **2017**, *22*, 713–725.
[55] E. v. Lenthe, E. J. Baerends, J. G. Snijders, *J. Chem. Phys.* **1993**, *99*, 4597–4610.
[56] E. van Lenthe, E.-J. Baerends, J. G. Snijders, *J. Chem. Phys.* **1994**, *101*, 9783–9792.
[57] E. van Lenthe, A. Ehlers, E.-J. Baerends, *J. Chem. Phys.* **1999**, *110*, 8943–8953.
[58] A. Klamt, *J. Phys. Chem.* **2002**, *99*, 2224–2235.
[59] J. Kieffer, D. Karkoulis, *J. Phys. Conf. Ser.* **2013**, *425*, 202012.
[60] A. D. Becke, *Phys. Rev. A Gen. Phys.* **1988**, *38*, 3098–3100.
[61] J. P. Perdew, W. Yue, *Phys. Rev. B* **1986**, *33*, 8800–8802.
[62] C. C. Pye, T. Ziegler, *Theor. Chem. Acc.* **1999**, *101*, 396–408.

Manuscript received: June 28, 2024
Accepted manuscript online: August 12, 2024
Version of record online: October 2, 2024